JOURNAL OF GEOPHYSICAL RESEARCH, VOL. ???, NO. , PAGES 1–25,

Generation mechanism for the intraseasonal variability in the Indo-Australian basin

Z. Yu and J. Potemra

International Pacific Research Center, University of Hawaii, Honolulu,

Hawaii, USA

Z. Yu, IPRC/SOEST, 1680 East-West Road, POST Building #413A, University of Hawaii, Honolulu, HI 96822, USA. (zuojun@hawaii.edu)

Abstract.

In the Indo-Australian basin, the strongest intraseasonal variability occurs during the second half of the year according to satellite altimeter data. This study attemps to identify the generation mechanism of this variability by means of numerical ocean modeling. By separately varying winds and transports through individual straits, it is shown that the seasonal cycles of both the wind and the transport through the Lombok Strait play crucial roles in generating mixed barotropic and baroclinic instabilities during July–September. Both the spatial and temporal patterns of the variability are also sensitive to transports through the Ombai Strait and the Timor Passage, though to a lesser degree. The Smagorinsky scheme in the model is essentail for these instabilities to reach the observed magnitude of standard deviation in sea-level anomaly; constant eddy viscosity, which needs to be sufficiently large for the Somali Current in summer, would damp the eddies in the Indo-Australian basin severely.

1. Introduction

This study concerns a region in the eastern Indian Ocean near the exit of the Indonesian throughflow (ITF), a region roughly from 100°E to 125°E and 20°S to 5°S. We will refer to the region as the Indo-Australian basin (IAB). Several currents due to various forcing mechanisms co-exist in the IAB. They are the ITF, the South Equatorial Current (SEC), the Eastern Gyral Current (EGC), the Leeuwin Current (LC), and the South Java Current (SJC). A schematic of these currents along with bathymetry is shown in Figure 1.

The ITF enters the IAB from the north and east via a limited number of small gaps within the Indonesian archipelago, namely the Lombok Strait, the Ombai Strait, and the Timor Passage. Since the bulk of the transport occurs in the upper 500 m [*e.g.*, *Potemra et al.*, 2002], the velocities in the straits can be large. *Hautala et al.* [2001] measured flows of almost 1 $m\,s^{-1}$ in the Lombok Strait, 0.5 $m\,s^{-1}$ in the Ombai Strait, and 0.25 $m\,s^{-1}$ in the Timor Passage. Since the Pacific water comes from the warmpool region, it is relatively warm and fresh in the upper ocean. Recent observations, however, suggest that the transport-weighted temperature through Makassar Strait is not as warm as previously thought due to buoyancy controls at the southern end of the strait [*Gordon et al.*, 2003]. The potential influence of this on the outflow is unclear. There are also significant tidal flows through these straits (*e.g. Ffield and Gordon* [1992]), but they are beyond the scope of the present study.

Observations of the ITF suggest a mean transport of approximately 8 Sv into the IAB [*Hautala et al.*, 2001]. Figure 2 shows collectively a few year-long observations through these straits. Among them are monthly-mean depth-integrated transport through the Lombok Strait during 1986 by *Murray and Arief* [1988], measurements taken at the Timor

Passage during 1992/93 by *Molcard et al.* [1996], and measurements at the Ombai Strait during 1996 by *Molcard et al.* [2001]. Note that the moorings were in the straits during different years. Each data set is shown along with its fit to an annual and semiannual harmonic to give an indication of the seasonal cycle, at least for the individual year surveyed. Maximum outflow is estimated during July–October, when local monsoon winds are from the southeast.

The ITF transport is not only influenced by local winds, but by remote Pacific forcing and large-scale waves generated in the Indian Ocean as well. All of these forcing processes undergo interannual variations, and thus the ITF has associated interannual variability. For example, observations show that ITF is weaker during El Niño events [*Meyers*, 1996; *Ffield et al.*, 2000; *Potemra et al.*, 2002].

Another component to the circulation in the IAB is the SJC, a coastal current that runs along the southern shore of Sumatra/Java and is influenced strongly by the coastal Kelvin waves. *Quadfassel and Cresswell* [1992] showed an eastward flow along Sumatra/Java between 100°E and 120°E from November through April, and a reversed flow between 105°E and 120°E during the rest of the year. More recent observations from a year-long mooring off Sumatra showed a flow to the southeast off south Java, with occasional reversals to the northwest [*Sprintall et al.*, 1999]. At least one of these reversals was attributed to a coastal Kelvin wave by *Sprintall et al.* [2000].

The ITF joins the SEC in the IAB, which becomes a broad westward flow between about 20°S and 10°S in the central Indian Ocean [*Cutler and Swallow*, 1984]. Estimates of mean transport in the SEC have been made using geostrophy along several sections between 60°E and 100°E and range from 25 to 40 *Sv* [*Schott et al.*, 1988; *Stramma and*

Lutjeharms, 1997]. More recent estimates by *Qu and Meyers* [2005] show that the SEC along 105°E is centered at 11°S and confined to the upper 350 m; the flows below 350-m depth are less than 2 cm/s (their Figure 4a). Their results also show stronger westward surface flows in August, which is consistent with the fact that the ITF is the strongest and the SJC flows westward during the period.

1.1. Eddy observations

Figure 3 shows sea-level anomalies of a single, 10-day composite from the TOPEX/Poseidon (T/P) altimeter (with long-term mean removed). Eddies can be easily identified as blue and red patches on both flanks of the SEC, suggesting the existence of barotropic instabilities associated with meridional shears. Note that the blue patches, indicative of cyclonic eddies, appear to the west of the Lombok Strait. An earlier study by Bray *et al.* [1997] focused on eddy features in the region. Direct observations of velocity along the IX-1 line (a track between Australia and Indonesia) show that these eddies are mainly confined to the upper 500 m [*Sprintall et al.*, 2002].

Satellite altimeter data was used by *Feng and Wijffels* [2002] to show intraseasonal variability in the IAB (Figure 4; a reproduction of their Figure 3c). The variability was strongest during the second half of the year (see their Figure 3), which coincides with the time of maximum ITF transport seen in Figure 2. Interestingly, the maximum standard deviation was located to the west of the Lombok Strait. The intraseasonal variability had a westward phase speed of 15–19 $cm\ s^{-1}$ and dominant periods between 40 and 80 days.

1.2. Eddy dynamics

Based on their continuously stratified quasigeostrophic model, *Feng and Wijffels* [2002] attributed baroclinic instabilities as the main cause of these eddies but acknowledged not having adequate data to examine the possibility of barotropic instabilities. This is consisitant with *Qiu et al.* [1999], who attributed their failure of reproducing the intrasonal variability in the IAB to their $1\frac{1}{2}$-layer model system, which disallows the baroclinic instability. On the other hand, *Nof et al.* [2002] used a nonlinear theory based on conservation of potential vorticity to show that the anticyclonic eddies in the IAB were driven by the β-effect. The region, in their opinion, had no mean state, therefore no instabilities associated with the mean state. They backed up their theory with $1\frac{1}{2}$-layer-model experiments. The study did not mention the cyclonic eddies that appear on the northern flank of the SEC (as indicated in Figure 3 by the blue patches).

1.3. Present research

The focus of this study is on the generation mechanism of the intraseasonal variability as revealed by satellite altimeter data [*Feng and Wijffels*, 2002]. We will show that the variability in the IAB is a mixed type of barotropic and baroclinic instabilities, and that the spatial and temporal structure of the varibility is strongly affected by wind stresses and by the branch of the ITF through the Lombok Strait.

2. Ocean model

The model is similar in many ways to the $4\frac{1}{2}$-layer system described in Han *et al.* [1999] and Han and McCreary [2001]. The differences from that system are given in detail by *Yu and McCreary* [2004]. Basically, the model consists of four active layers with variables

of thicknesses h_i, velocities $\mathbf{v}_i$, salinities S_i, and temperatures T_i (layer index $i = 1$, 2, 3, or 4), overlying a deep, inert ocean where the pressure gradient vanishes (a $4\frac{1}{2}$-layer system). Each of the layers represents water generated primarily by a specific process, and hence corresponds mostly to a single water-mass type: Layer 1 is the surface mixed layer, determined by Kraus-Turner [1963] physics, modified to include the parameter n for cooling efficiency [*Niiler and Kraus*, 1977]; layer 2 is the seasonal thermocline; layers 3 and 4 represent thermocline and upper-intermediate waters, respectively. To simulate the processes of upwelling, subduction and diapycnal mixing, fluid is allowed to transfer across the interfaces between adjacent layers. When this occurs, mass, heat and salt remain conserved.

2.1. Model basin, initial conditions, and spin up

The model basin is a representation of the Indian Ocean north of 30°S and from 30°E to 125°E based on ETOPO5. To determine the basin boundaries, model grid points are taken to be land wherever the ocean depth is shallower than 200 m. We specify ITF transports through three major straits, namely the Lombok Strait, the Ombai Strait, and the Timor Passage, and details on model boundary conditions will be given in Section 2.4.

The model grid is in spherical coordinates with $\Delta x = \Delta y = 0.1°$, and the integration time step is usually $\Delta t = 10$ minutes. This resolution was chosen because the Lombok Strait is about 35 km wide. Initial temperature and salinity fields in each layer are the mean climatological fields taken from World Ocean Atlas 1998 [WOA98; *Conkright et al.*, 1998] at depths of 20, 50, 200, and 600 m, respectively. The model is spun up from a state of rest for 4 years, by which time the solutions' surface fields have very nearly adjusted to their equilibrium states. Most experiments reported in this study are listed in Tables 1

and 2; each with its unique setup and is integrated from this equilibrium state for another 3 years (model years 5–7). The fields used for analyses are based on 3-day sampling of the output from model years 5–7, with a focus on model year 6. When the seasonal mean needs to be removed, it is done by removing a 90-day running mean from the total field.

2.2. The Smagorinsky Diffusivity

For the success of this study, the most important addition to the model is the Smagorinsky diffusivity for horizontal diffusion [*Smagorinsky*, 1963, 1993]. The Smagorinsky formula is,

$$A_M = C\Delta x\Delta y[(\partial u/\partial x)^2 + \tfrac{1}{2}(\partial v/\partial x + \partial u/\partial y)^2 + (\partial v/\partial y)^2]^{\frac{1}{2}}, \quad (1)$$

where C (the HORCON parameter) is recommended to be in the range of 0.1 to 0.2 [*Mellor*, 2002]. The advantages of the Smagorinsky scheme are that C is non-dimensional, that A_M decreases as model horizontal resolution improves, and that A_M is small (large) if velocity gradients are small (large). An example will be given in Section 3.5 to show that the Smagorinsky scheme is essential for simulating energetic eddies in the IAB when the model domain contains other swift currents.

2.3. Interior forcing

Because the model is thermodynamically active, surface boundary conditions include forcing by heat, freshwater and momentum fluxes. Climatological monthly-mean air temperature and specific humidity, together with the model's T_1 field, are used in the calculation of sensible and latent heat fluxes, as in *McCreary and Kundu* [1989] and *McCreary et al.* [1993]. The forcings for our main-run solution (defined in Section 3), except for the wind stresses, are all taken from the Comprehensive Ocean-Atmosphere Data Set

prepared at the University of Wisconsin-Milwaukee (COADS/UWM), constrained as recommended by the authors based on a global budget obtained from an oceanic general circulation model [*da Silva et al.*, 1994]. Specifically, we use 93% of the shortwave radiation (Q_{sw}) and 112% of the precipitation. The monthly-mean climatology of the wind stresses for the main run is based on surface winds from the European Centre for Medium-Range Weather Forecasts (ECMWF) for October 1992–December 1998, to coincide with the T/P period used by *Feng and Wijffels* [2002]. It will be shown in Section 3.2 that the spatial distribution of the sea-level change and the magnitude of the variability are very sensitive to winds.

2.4. Indonesian throughflow

Closed, no-slip conditions, $u_i = v_i = 0$, are imposed on all basin boundaries, except at inflow/outflow ports. The artificial southern boundary is also closed (to ensure that the system conserves mass), and the temperature and salinity in layers 3 and 4 are relaxed back to their mean climatologies south of 25°S to make up for missing inflows at these depths.

To studying the impact of the ITF, inflows are allowed through segments of the boundary at the Lombok Strait, the Ombai Strait, and the Timor Passage. The total inflow M will be balanced by an outflow of equal amount of transport through the southern boundary near the southwest corner at depth. Specifically, the boundary conditions for the ITF are:

$$v_1 = -\phi_1 \frac{M_{Lombok}}{h_1 L_{Lombok}}, v_2 = -\phi_2 \frac{M_{Lombok}}{h_2 L_{Lombok}}, v_3 = v_4 = 0, \tag{2}$$

$$u_1 = -\phi_1 \frac{M_{Ombai}}{h_1 L_{Ombai}}, u_2 = -\phi_2 \frac{M_{Ombai}}{h_2 L_{Ombai}}, u_3 = -\phi_3 \frac{M_{Ombai}}{h_3 L_{Ombai}}, u_4 = 0, \tag{3}$$

$$u_1 = -\phi_1 \frac{M_{Timor}}{h_1 L_{Timor}}, u_2 = -\phi_2 \frac{M_{Timor}}{h_2 L_{Timor}}, u_3 = -\phi_3 \frac{M_{Timor}}{h_3 L_{Timor}}, u_4 = 0, \tag{4}$$

and at the southern boundary

$$v_1 = v_2 = 0, v_3 = \frac{1 - M_{Lombok} - M_{Ombai} - M_{Timor}}{h_3 L_S}, \quad v_4 = -\frac{1}{h_4 L_S}, \tag{5}$$

where M_{str} is the specified transport through a particular strait (str) of width L_{str}, and $L_S = 7.5°$ for the outflow. Conditions (2)–(5) require that the model ITF enters the IAB in layers 1–3, whereas the compensating outflow leaves the model domain in layers 3 and 4. Therefore, $\phi_1 + \phi_2 + \phi_3 = 1$, except at the shallow Lombok Strait where $\phi_1 + \phi_2 = 1$ so that the inflow comes in through layers 1 and 2 only. Unlike L_{str}, the choice of L_S is rather arbitrary and the solutions are not sensitive to its width according to earlier studies by *McCreary and his collaborators*. Transport M_{str} is either the seasonal cycle from observations or an idealized value selected for sensitivity study (Table 1).

The temperature and salinity at the inflow ports are (T_1, T_2, T_3, T_4)=(28.5, 27, 16, 7.2)°C and (S_1, S_2, S_3, S_4)=(33.8, 34.3, 34.7, 34.5) psu, unless stated otherwise. The values are taken after *Yu and McCreary* [2004]. The sensitivity to inflows' T/S, including their seasonal cycles, will be discussed in Section 3.4.

2.5. Virtual runoff

In the Indian Ocean, runoff, as well as the ITF, is crucial for the system to sustain its long-term mean sea surface salinity (SSS) distribution. Since accurate runoff data is not available, its effects are parameterized by nudging model surface salinity (S_1) to observed SSS at basin boundaries when $S_1 >$ SSS [*Yu and McCreary*, 2004]. This approach can be viewed as conditioned restoring of model surface salinity along the coastlines. We will not go into more details here, because the intraseasonal variability in the IAB is primarily dynamically driven as we will see shortly.

3. Model results:

The mean surface circulation of the IAB is fairly well simulated by the model, which includes the SEC, EGC, LC, and SJC (Figure 1). Of the most importance is the SEC, as we will see shortly its role in generating instabilities. The model SEC is centered along 11°S and confined to the upper 3 layers (about 300 m). This is consistant with the observations by *Qu and Meyers* [2005; their Figure 4a]. However, the annual-mean magnitude of the model SEC in the upper 100 m can reach 20 cm/s at 105°E, about twice as strong as reported by *Qu and Meyers* [2005]. Such a magnitude in modeled SEC is common, as shown by Figure 6 of *Du et al.* [2005], which is based on an OGCM for the Earth Simulator (OFES; *Masumoto et al.*, [2004]). Since there is a lot of smoothing involved when using *in situ* data, the observed SEC could be underestimated.

Next, we will describe our main run (Exp. A0 in Table 1), an experiemnt forced by observed seasonal cycles of transport through the three straits (thicker lines in Figure 2), as well as by the ECMWF winds from the period of October, 1992–December 1998. We will then present a series of controlled experiments that are designed to identify the importance of wind forcing (Exps. W1 and W2 in Table 2), as well as of transport at each strait (Exps. A1–A6 in Table 1), in generating instabilities in the IAB.

3.1. Main run (Exp. A0)

The top panel of Figure 5 shows the standard deviation of sea-level anomaly during July–September with seasonal-mean removed. Comparing to Figure 4 by *Feng and Wijffels* [2002], the agreement is fairly good in terms of spatial pattern and magnitude, except for the longitudional location of the maximum variability. As we will see shortly that the sea-level variability, which reflects instabilities in the system, is quite sensitive to various

aspects of the forcing, so such a disagreement between the model and the observation is not too surprising.

A snapshot of surface flows from the main run is shown in the top panel of Figure 6. In order to show the seasonal variations of these eddies, we define layer-1 eddy kinetic energy, EKE $= \frac{1}{2}(u_1'^2 + v_1'^2)$, as a measure of eddy activity in the region. [Alternatively, we could define EKE to be $\frac{1}{2}(u_1'^2 + v_1'^2)h_1$, or to include the layer-2 contribution as well.] The perturbation here is in reference to the seasonal mean. The EKE is averaged from 102°E to 115°E and from 14°S to 9°S (the red box in the top panel as well as in Figure 5). This box is selected to cover the region of high sea-level variability based on Figure 3c of *Feng and Wijffels* [2002], and to exclude the immediate vicinity of the Lombok Strait. It is clear that the eddies in the main run are more active during the second half of the year (black curve in the middle panel), just as in the T/P observation. Note that the intraseasonal variability in the model simulation may not be precisely captured using the EKE defined above, because the spatial distribution of eddies may not be confined in the selected box when forcings and other parameters are changed. This will become obvious when we discuss test cases in Sections 3.2 and 3.3.

To understand how the inflows affect the sea-level variability, we examine the currents in layer 1, among other things. As M_{Lombok} and M_{Lombok} increase during June–August, the SEC and its meridional shears increase correspondingly. As a result, $(\frac{\partial^2 U_1}{\partial y^2} - \beta)$, where U_1 is averaged between 110°E and 115°E, indicates a condition in favor of barotropic instability (bottom panel of Figure 6). The same calculation, if performed west of 100°E, would suggest little barotropic instability. Therefore, the inflows strengthen the SEC and enhance the meridional shears on its flanks.

Now, let's examine the energy conversions during the growth period of the main run, marked by red vertical lines in the middle and bottom panels of Figure 6. The barotropic conversion,

$$C_1 = -\sum_{i=1}^{4}[\overline{u_i'v_i'}(\overline{u_i}_y + \overline{v_i}_x)\overline{h_i} + \overline{u_i'u_i'}\overline{u_i}_x\overline{h_i} + \overline{v_i'v_i'}\overline{v_i}_y\overline{h_i}], \tag{6}$$

is dominated by the terms in the two upper layers (see *McCreary and Yu* [1992] for derivation of these terms in a $2\frac{1}{2}$-layer system). The overbar is time-averaging over the specified growth period. The maximum barotropic conversion locates just south of the Lombok Strait, and extends southwestward (upper panel of Figure 7). In addition, there exist two secondary maxima west and south of Sumbar Island, respectively. The baroclinic conversion,

$$\begin{aligned} C_3 = \; & -g\overline{h_1'\mathbf{v_1'}} \cdot (\boldsymbol{\nabla}\overline{h_1}\overline{\rho_{51}} + \boldsymbol{\nabla}\overline{h_2}\overline{\rho_{52}} + \boldsymbol{\nabla}\overline{h_3}\overline{\rho_{53}} + \boldsymbol{\nabla}\overline{h_4}\overline{\rho_{54}}) \\ & -g\overline{h_2'\mathbf{v_2'}} \cdot [\boldsymbol{\nabla}(\overline{h_1} + \overline{h_2})\overline{\rho_{52}} + \boldsymbol{\nabla}\overline{h_3}\overline{\rho_{53}} + \boldsymbol{\nabla}\overline{h_4}\overline{\rho_{54}}] \\ & -g\overline{h_3'\mathbf{v_3'}} \cdot [\boldsymbol{\nabla}(\overline{h_1} + \overline{h_2} + \overline{h_3})\overline{\rho_{53}} + \boldsymbol{\nabla}\overline{h_4}\overline{\rho_{54}}] \\ & -g\overline{h_4'\mathbf{v_4'}} \cdot \boldsymbol{\nabla}(\overline{h_1} + \overline{h_2} + \overline{h_3} + \overline{h_4})\overline{\rho_{54}}, \end{aligned} \tag{7}$$

is also a source in the model, though somewhat weaker than its barotropic counterpart. Therefore, the eddies in the main run are a mixed type of instabilities in their generation region, roughly from 108°E to 116°E and 9°S to 13.5°S.

The phase speeds of the eddies are estimated using intraseasonal sea-level change along 10°S (left panel of Figure 8) and 12°S (right panel). The red vertical lines mark 108°E and 116°E, respectively, roughly the edges of the generation region as determined by energy conversions in Figure 7, so the eddies to the west of 108°E can be considered as free waves. At 12°S, the phase speed is 18 cm/s west of 108°E and varies between 12 cm/s and 17 cm/s east of 116°E. These phase speeds are similar to those quoted by *Feng and Wijffels* [2002] based on T/P data. It is worth noting that the same phase information can also be obtained by using layer-1 meridional currents, except with a 90° phase shift.

East of 116°E, there is little activity along 10°S, while variability along 12°S are likely due to westward propagating eddies generated south of Sumbar Island.

3.2. Sensitivity to winds (Exps. W1 and W2)

The intraseasonal variability in the IAB varies from year to year according to analysis of T/P observations by *Feng and Wijffels* [2002] (see their Figure 7a). It would be very difficult for the model to reproduce the time series of the T/P observation, for we do not have observed transports at each strait year after year, nor the actual wind observations. Instead, we will show model sensitivity to climatological winds in this section and to idealized transports in the following section.

Figure 5 compares spatial distributions of sea-level variability during July–September, while the middle panel of Figure 6 compares their corresponding EKE during model year 6, of the simulations forced by three sets of monthly-mean climatology based on different periods of the ECMWF wind product. The variability seems to be much weaker when forced by monthly-mean winds based on the longer period of 1986–2003 (middle panel of Figure 5 and the red curve in Figure 6), which would easily be one's preference as climatological forcing because of its record length. Only a very small area centered around 103°E and 12°S has a standard deviation exceeding 5 *cm*. [The variability is even weaker if the model is forced by COADS winds. In this case, the only area barely reaching 5-*cm* standard deviation is located near 116°E and 14°S (not shown).] On the other hand, the model simulation for the more recent period of 1998-2003 (bottom panel of Figure 5) is much closer to the T/P observation than the main run does, in terms of the spatial distribution and magnitude of the standard deviation. This is consistent with the general consensus that the quality of ECMWF winds has improved during the 1990s (*e.g. Yu et*

al. [2000]). Therefore, we should avoid using the ECMWF wind in the late 1980s, and the COADS winds, in modeling the variability in the IAB.

The cause for the differences among Exps. A0, W1, and W2 may be local or remote. The wind analysis show that the local zonal wind is much weaker in Exp. W1 than that in both Exps. A0 and W2. For Exp. W1, the $(\frac{\partial^2 U_1}{\partial y^2} - \beta)$ contours are more confined to north of 11°S, so is the C1 term for barotropic instability; the C3 term is negligible (not shown). Therefore, the relatively weak local zonal wind is believed to be the cause of a weaker SEC, thus the weakened intraseasonal sea-level variability in Exp. W1.

The local zonal winds are very similar for Exps. A0 and W2, resulting in similar plots of $(\frac{\partial^2 U_1}{\partial y^2} - \beta)$ and C1. However, the baroclinic C3 term for Exp. W2 is spread further to the west and to the south than that for Exp. A0 inside the box shown at the bottom panel of Figure 7. The dominant component for such a distribution in C3 is $\overline{h_1' v_1'}$. We are unable to pin down the cause, which could be remotely forced, or by slightly enhanced local meridional wind in Exp. W2.

3.3. Sensitivity to transport via each strait (Exps. A1–A6)

A possible linkage between the intraseasonal variability in the IAB and the transport of the ITF is suggested by the fact that the strongest variability appears during a time when transports at the Lombok and Ombai Straits reach their peaks (Figure 2). To illustrate the impact of seasonal cycle in M_{Lombok}, we first replaced the observed M_{Lombok} used in the main run by a constant $M_{Lombok} = 1$ Sv. The level of EKE is greatly reduced (the red curve in the top panel of Figure 9). Note that there is little phase shift of the EKE peak, only its magnitude is weakened. Clearly, the seasonal cycle of the variability left in the system is due to the seasonal cycle of the winds, plus that of the transport via the

Ombai Strait. When we force the model with $M_{Lombok} = 3$ Sv, the EKE level is elevated throughout the year (the blue curve in the top panel). In both Exps. A1 and A2, the EKE change (therefore the change in sea-level variability) is related to change in the SEC, the meridional shears on its flanks, and the condition for barotropic instability, as we set M_{Lombok}= 1 Sv or M_{Lombok}= 3 Sv throughout the year. The $(\frac{\partial^2 U_1}{\partial y^2} - \beta)$ plot indicates a much less favorable condition for the barotropic instability during July–September in Exp. A1 with contours confined to north of 11°S, while $(\frac{\partial^2 U_1}{\partial y^2} - \beta)$ changes signs all year round to as far south as 14°S in Exp. A2 (not shown). **Consequently, the C_1 term is much weaker in Exp. A1 and a little stronger in Exp. A2 than that in Exp. A0. The character of mixed instabilities remains true even when M_{Lombok} varies, because the C_3 term (dominated by $-g\overline{h_1' v_1'}\ \overline{h_1}_y \overline{\rho_{51}}$) responds to M_{Lombok} in the same way as the C_1 term does.** Two additional experiments were carried out in which the observed M_{Lombok} was shifted by 2 months, the peak in EKE was shifted accordingly (not shown). So, we conclude that the seasonal cycle in the observed M_{Lombok} is very important to the strength and timing of the observed variability.

Now, let's consider a case of constant $M_{Ombai} = 4$ Sv. The peak of EKE is reduced (the red curve in the middle panel of Figure 9), suggesting that M_{Ombai} be more than 4 Sv during July–September. On the other hand, a constant transport of 4 Sv during the rest of the year does not seem to affect EKE much. Similarly, the EKE is affected during September–December when $M_{Timor} = 4$ Sv is used instead of the observed one, but not during other months (the blue curve in the middle panel).

Finally, we present two cases when the Lombok Strait is either closed (Exp. A5) or its width is doubled (Exp. A6) in the model. Most of the global oceanic general circulation

models (OGCMs) cannot resolve the narrow Lombok Strait, and Exps. A5 and A6, though unrealistic, are designed to test the potential impact of such model details. In Exp. A5, the observed M_{Lombok} is added to the Ombai Strait; as a result, the standard deviation is shifted southward (top panel of Figure 10). In Exp. A6, the observed M_{Lombok} is unchanged; the widened Lombok Strait causes a 40% reduction in EKE (not shown) and weakens the standard deviation of sea-level anomaly as well (middle panel of Figure 10). Therefore, a proper representation of the Lombok Strait in the model is important for reproducing the observed sea-level variability in the IAB.

3.4. Sensitivity to inflows' T/S (Exp. A7)

Since the intraseasonal sea-level variability is caused by mixed instabilities in the model, one may ask what the sensitivity would be if the inflows are warmer and fresher, or vice versa. We can expect the inflows' T/S to affect the baroclinicity of the system. Indeed, the C3 term is enhanced when layer-1's T/S at the inflow ports are made warmer and fresher by 1°C and 0.5 *psu*. Unlike the sensitivity to transports at the ports, the sensitivity to inflows' T_1/S_1 can be seen as long as one of the straits' T_1/S_1 is modified. There is no preference over any one particular strait. The opposite happens when T_1/S_1 at the inflow ports are made cooler and saltier.

Since we don't have T/S data associated with the transports shown in Figure 2, we turn to other sources. The newest dataset for the region is called CARS, CSIRO Atlas of Regional Seas (*Dunn and Ridgway*, [2002]). We examined the seasonal cycle of T/S at the 3 straits, and made Exp. A7 using the top 50-m T/S as inflows' T_1/S_1 and assumed T_2=T_1-1.5°C at the ports. The inflows' T_1/S_1 in Exp. A7 has a distinct annual cycle: At the Lombok Strait, T_1 peaks at 28.5°C during February–March and drops to 25.5°C

during July–October. The T_1 at Ombai and Timor has the same annual cycle as that at the Lombok, but 1°C warmer throughout the year. The S_1 at the Lombok Strait is freshest at 33.6 *psu* during February–May and rises to 34 *psu* in June and to 34.4 *psu* in September. The S_1 is nearly identical at Ombai and Timor , but is freshest at 34 *psu* in June and rises to 34.5 *psu* during November–January. So, Exp. A7 has cooler and saltier inflows than Exp. A0 during June–August, the instability growth period, which should weaken the baroclinic instability via the C3 term. Indeed, this is the case as shown by the drop of EKE level (red curve in the bottom panel of Figure 9). It is worthy noting that the annual cycle of inflows' T_1/S_1 in Exp. A7 actually lessens the impact of cooler T_1 and saltier S_1 on the growth of instabilities than persistantly cooler and saltier (constant) inflows would have had.

3.5. Sensitivity to eddy viscosity ν_2

Here, we show one last test case to illustrate the importance of non-uniform eddy viscosity in simulating the intraseasonal variability in the IAB. The strong western boundary current in the Indian Ocean, the Somali Current, prohibits us from lowering constant ν_2 to any value smaller than 5×10^6 cm^2/s under the current model grid. However, $\nu_2 = 5 \times 10^6$ cm^2/s is too large to allow energetic eddies at 0.1° horizontal resolution [*e.g. Yu et al.*, 2003]. As is indeed the case here when the minimum eddy viscosity is kept at 5×10^6 cm^2/s: The EKE is greatly reduced (blue curve in the bottom panel of Figure 9); its standard deviation of sea-level anomaly is lowered and its center is shifted shouthward (bottom panel of Figure 10; note that this shift is partly the cause of the EKE reduction in the red box). Therefore, the Smagorinsky scheme is crucial for obtaining a realistic IAB simulation when other swift currents exist in the model domain.

4. Summary and discussion

In this study, we use an ocean model as a tool to study the generation mechanism of the intraseasonal sea-level variability in the IAB. We have shown that the variability is sensitive to all aspects of the forcing, in particular the wind (Section 3.2) and the transport via the Lombok Strait (Section 3.3). We hope that these modeling results will benefit OGCMs in their designs, their choice of wind forcing as well as mixing parameterizations. The results, of course, need to be validated by future observations, as may be obtained by the on-going International Nusantara Stratification and Transport Program (INSTANT) program. In particular, there exists intraseasonal variability in winds and in transport via each strait. Such variability, if included in the model, may enhance the sea-level variability. However, we believe the fundamental mechanism behind the observed sea-level intraseasonal variability is the mixed instabilities due to the mean ocean state, a main conclusion of this study.

Acknowledgments. This study was supported by NASA through grant #NAG 5-10045 and by the Japan Agency for Marine-Earth Science and Technology (JAMSTEC) through its sponsorship of the International Pacific Research Center (IPRC). The assistance of the Ferret group at NOAA/PMEL is greatly appreciated. Comments from Ming Feng and Jay McCreary, as well as the two reviewers, were extremely helpful in improving the manuscript. This paper is IPRC Contribution No. xxx and SOEST No. xxxx.

References

Bray, N. A., S. E. Wijffels, J. C. Chong, M. Fieux, S. Hautala, G. Meyers, and W.M.L. Morawitz, 1997: Characteristics of the Indo-Pacific throughflow in the eastern Indian

Ocean. *Geophys. Res. Lett.*, **24**, 2569–2572.

Conkright, M., S. Levitus, T. O'Brien, T. Boyer, J. Antonov, and C. Stephens, 1998: *World Ocean Atlas 1998 CD-ROM Data Set Documentation. Tech. Rep.* 15, NODC Internal Report, 16pp, Silver Spring, MD.

Cutler, A.N. and J.C. Swallow, 1984: Surface currents of Indian Ocean. *I. O. S. Technical Report 187.*

da Silva A., A.C. Young, and S. Levitus, 1994: Atlas of Surface Marine Data 1994, Volume 1: Algorithms and Procedures. NOAA Atlas NESDIS **6**, U.S. Department of Commerce, Washington, D.C.

Du, Y., T. Qu, G. Meyers, Y. Masumoto, and H. Sasaki, 2005: Seasonal heat budget in the mixed layer of the southeastern tropical Indian Ocean in a high-resolution ocean general circulation model, *J. Geophys. Res.*, **110**, C04012, doi:10.1029/2004JC002845.

Dunn J.R., and K.R. Ridgway, 2002: Mapping ocean properties in regions of complex topography, *Deep Sea Research I: Oceanographic Research*, **49 (3)**, 591–604.

Feng, M. and S. Wijffels, 2002: Intraseasonal variability in the South Equatorial Current of the East Indian Ocean. *J. Phys. Oceanogr.*, **32**, 265–277.

Ffield, A., and A.L. Gordon, 1992: Vertical mixing in the Indonesian thermocline. *J. Phys. Oceanogr.*, **22**, 184–195.

Ffield, A., K. Vranes, A.L. Gordon, R.D. Susanto and S.L. Garzoli, 2000: Temperature variability within Makassar Strait, *Geophys. Res. Let.*, **27**, 237–240.

Gordon, A.L., R.D. Susanto and K. Vranes, 2003: Cool Indonesian throughflow as a consequence of restricted surface layer flow. *Nature*, **425**, 824–828.

Han, W., and J.P. McCreary, 2001: Modelling salinity distributions in the Indian Ocean. *J. Geophys. Res.*, **106**, 859–877.

Han W., J.P. McCreary, D.L.T. Anderson, and A.J. Mariano, 1999: On the dynamics of the eastward surface jets in the equatorial Indian Ocean. *J. Phys. Oceanogr.*, **29**, 2191–2209.

Hautala, S.L., J. Sprintall, J.T. Potemra, A.G. Ilahude, J.C. Chong, W. Pandoe and N. Bray, 2001: Velocity structure and transport of the Indonesian throughflow in the major straits restricting flow into the Indian Ocean. *J. Geophys. Res.*, **106**, 19,527–19,546.

Kraus, E.B. and J.S. Turner, 1967: A one-dimensional model of the seasonal thermocline: II. The general theory and its consequences, *Tellus*, **19**, 98–106.

Masumoto, Y., *et al.*, 2004: A fifty-year eddy-resolving simulation of the world ocean?Preliminary outcomes of OFES (OGCM for the Earth Simulator), *J. Earth Simulator*, **1**, 35–56.

McCreary, J.P. and P.K. Kundu, 1989: A numerical investigation of sea-surface temperature variability in the Arabian Sea, *J. Geophys. Res.*, **94**, 16,097–16,114.

McCreary, J.P. and Z. Yu, 1992: Equatorial Dynamics in a $2\frac{1}{2}$-layer Model, *Prog. in Oceanogr.*, **29**, 61–132.

McCreary, J.P., P.K. Kundu and R.L. Molinari, 1993: A numerical investigation of dynamics, thermodynamics, and mixed-layer processes in the Indian Ocean, *Prog. Oceanog.*, **31**, 181–224.

Mellor, G.L., 2002: Users guide for a three-dimensional, primitive equation, numerical ocean model (October 2002 version), *Prog. in Atmos. and Ocean. Sci.*, Princeton University, 42 pp.

Meyers, G., 1996: Variation of Indonesian throughflow and ENSO, *J. Geophys. Res.*, **101**, 12,255–12,264.

Molcard, R., M. Fieux and A.G. Ilahude, 1996: The Indo-Pacific Throughflow in the Timor Passage, *J. Geophys. Res.*, **101**, 12,411–12,420.

Molcard, R., M. Fieux and F. Syamsudin, 2001: The Throughflow within Ombai Strait. *Deep Sea Res., Part II*, **48**, 1237–1253.

Murray, S. P., and D. Arief, 1988: Throughflow into the Indian Ocean through the Lombok Strait, January 1985 - January 1986. *Nature*, **333**, 444–447.

Niiler, P.P., and E.B. Kraus, 1977: Chapter 10, One dimensional models of the upper ocean, *Modelling and prediction of the upper layers of the ocean, Edited by Kraus, Pergamon press, Oxford & New York.*

Nof, D., T. Pichevin and J. Sprintall, 2002: "Teddies" and the origin of the Leeuwin Current. *J. Phys. Oceanogr.*, **32**, 2571–2588.

Potemra, J.T., 1999: Seasonal variations of the Pacific to Indian Ocean throughflow. *J. Phys. Oceanogr.*, **29,** 2930-2944.

Potemra, J.T., S.L. Hautala, J. Sprintall and W. Pandoe 2002: Interaction between the Indonesian Seas and the Indian Ocean in observations and numerical models, *J. Phys. Oceanogr.*, **32**, 1838–1854.

Qiu, B., M. Mao, Y. Kashino, 1999: Intraseasonal variability in the Indo-Pacific throughflow and the regions surrounding the Indonesian Seas. *J. Phys. Oceanogr.*, **29**, 1599-1618.

Qu, T., and G. Meyers, 2005: Seasonal characteristics of circulation in the southeastern tropical Indian Ocean. *J. Phys. Oceanogr.*, **35**, 255–267.

Quadfassel, D., and G.R. Cresswell, 1992: A Note on the Seasonal Variability of the South Java Current. *J. Geophys. Res.*, **97**, 3685–3688.

Schott, F., M. Fieux, J. Kindle, J. Swallow and R. Zantopp, 1988: The boundary currents north and east of Madagascar. Part II: Direct measurements and model comparisons. *J. Geophys. Res.*, **93**, 4963–4974.

Smagorinsky, J., 1963: General circulation experiments with the primitive equations: I. The basic experiment. *Mon. Wea. Rev.*, **91**, 99–164.

Smagorinsky, J., 1993: Some historical remarks on the use of nonlinear viscosities. *Large Eddy Simulation of Complex Engineering and Geophysical Flows*, B. Galperin and S.A. Orszag, Eds., Cambridge University Press, 3–36.

Sprintall, J., J. Chong, F. Syamsudin, W. Morawitz, S. Hautala, N. Bray and S. Wijffels, 1999: Dynamics of the South Java Current in the Indo-Australian Basin, *Geophys. Res. Let.*, **26,** 2493–2496.

Sprintall, J., A.L. Gordon, R. Murtugudde and R.D. Susanto, 2000: A semi-annual Indian Ocean forced Kelvin wave observed in the Indonesian Seas in May 1997. *J. Geophys. Res.*, **105**, 17,217–17,230.

Sprintall, J., S. Wijffels, T. Chereskin and N. Bray, 2002: The JADE and WOCE I10/IR6 Throughflow sections in the southeast Indian Ocean. Part 2: velocity and transports. *Deep Sea Res. Part II*, **49**, 1363–1389.

Stramma, L., and J.R.E. Lutjeharms, 1997: The flow field of the subtropical gyre of the South Indian Ocean. *J. Geophys. Res.*, **102**, 5513–5530.

Yu, Z. and J.P. McCreary, 2004: Assessing precipitation products in the Indian Ocean using an ocean model. *J. Geophys. Res.*, **109**, C05013, doi:10.1029/2003JC002106.

Yu, Z., J.P. McCreary, W.S. Kessler, and K.A. Kelly, 2000. Influence of equatorial dynamics on the Pacific North Equatorial Countercurrent. *J. Phys. Oceanogr.*, **30**, 3179–3190.

Yu, Z., N. Maximenko, S.-P. Xie and M. Nonaka, 2003: On the Termination of the Hawaiian Lee Countercurrent. *Geophys. Res. Lett.*, **30(5)**, 1215, doi:10.1029/2002GL016710.

Exp.	Controlled inflows through Lombok, Ombai and Timor
A0	seasonal cycle of M_{Lombok}, M_{Ombai}, and M_{Timor} as observed
A1–A2	set $M_{Lombok} = 1\ Sv$ and $3\ Sv$, respectively
A3	set $M_{Ombai} = 4\ Sv$
A4	set $M_{Timor} = 4\ Sv$
A5	close Lombok Strait and add observed M_{Lombok} to Ombai Str.
A6	double Lombok Str. width, apply observed M_{Lombok}
A7	seasonal cycles of T_1/S_1 considered at all three straits

Table 1. Sensitivity to ITF transports and T/S. Prescribed inflows are based on observations unless stated otherwise. Each experiment in the A-series is forced by the same wind, namely the monthly-mean ECMWF winds based on Oct. 1992–Dec. 1998 period.

Exp.	Climatological winds
W1	monthly-mean ECMWF winds based on 1986–2003 period
W2	monthly-mean ECMWF winds based on 1998–2003 period

Table 2. Sensitivity to winds. Prescribed inflows are the same as in Exp. A0.

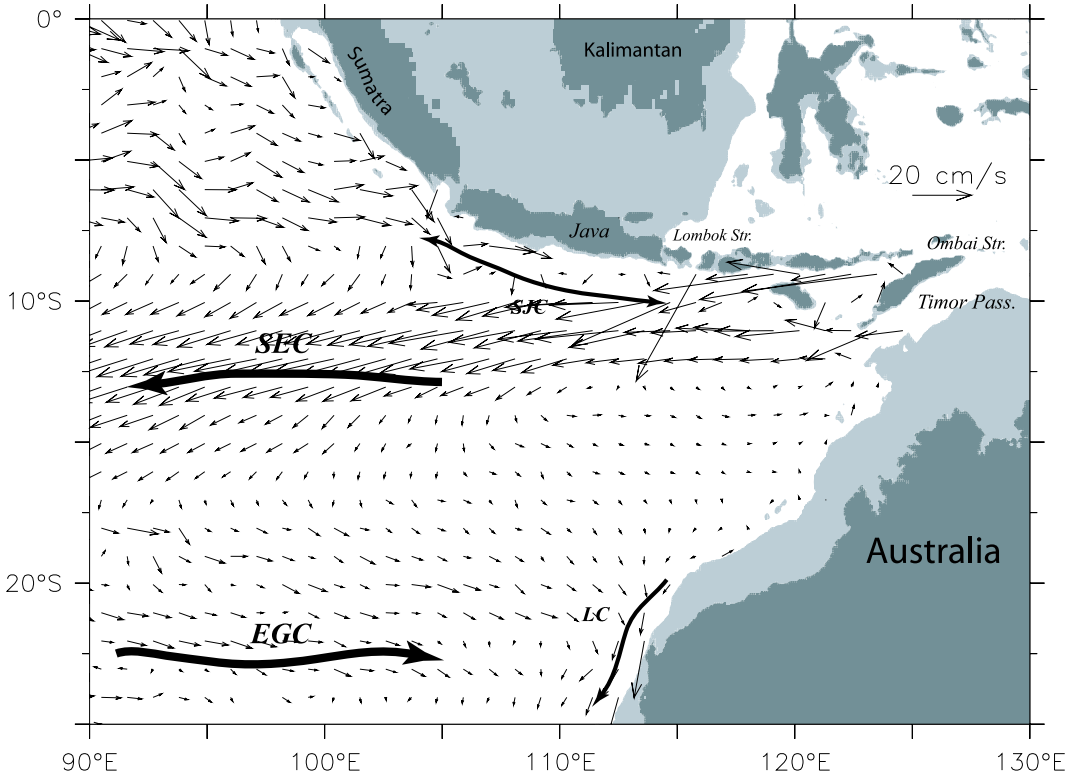

Figure 1. Topography and surface currents of the Indo-Australian Basin. The light shading marks depths less than 200 m, and the dark shading indicates the land. Also given are major currents and the main exit passages of the ITF: Lombok Strait, Ombai Strait and Timor Passage. Ocean currents are annual-mean surface flows from one of our test experiments.

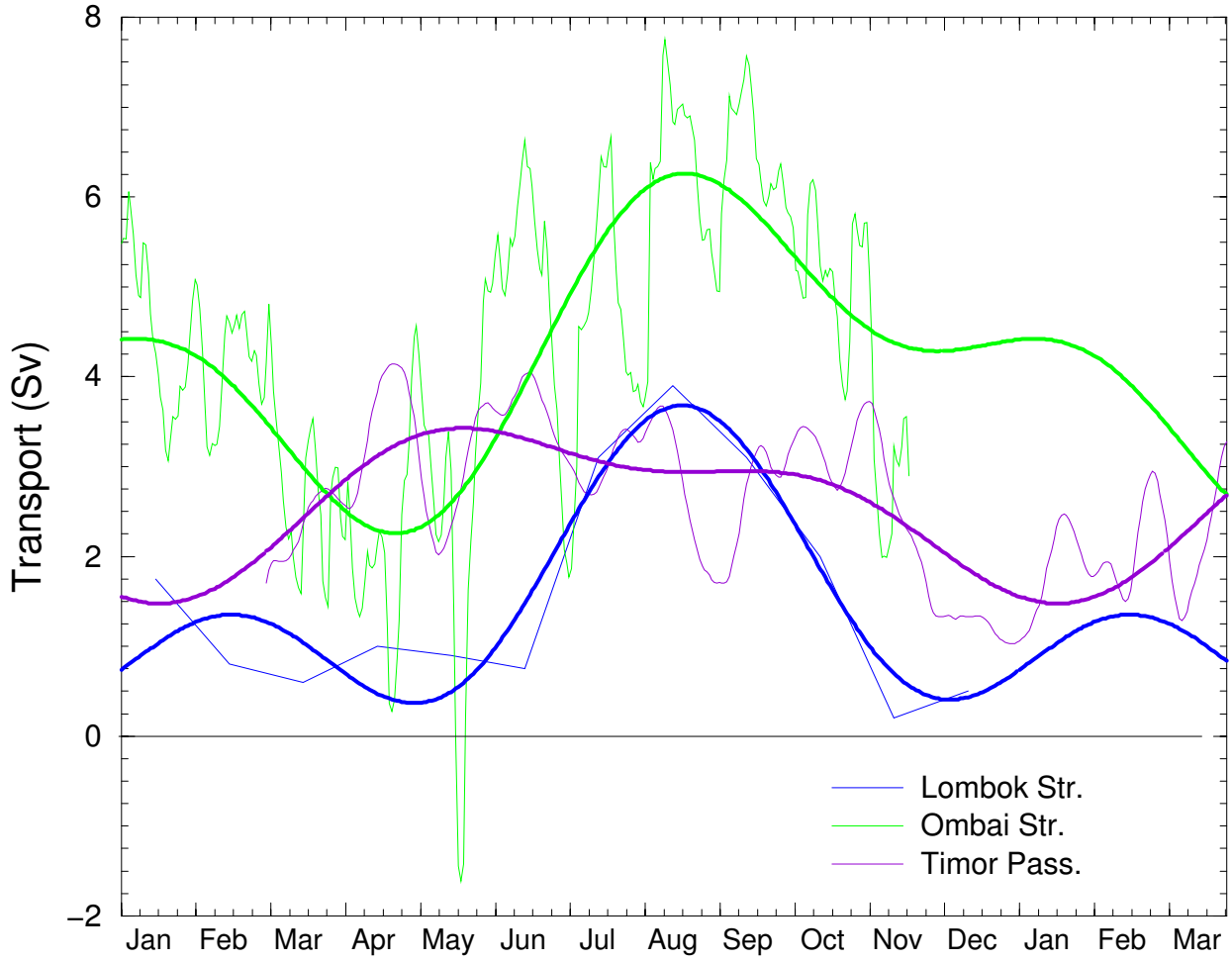

Figure 2. The transports from three different moorings in the three ITF exit straits are shown. The data from the Lombok Strait (blue) are monthly means for 1986, reproduced from *Murray and Arief* [1988]. The Ombai Strait measurements (green) are 15-day low-pass filtered transports from *Molcard et al.* [2001]. The upper 500-m transports for Timor Passage (purple) are taken from *Molcard et al.* [1996]. A seasonal cycle, estimated by a fit of the annual and semiannual harmonics, is given by a thicker smooth line of the same color.

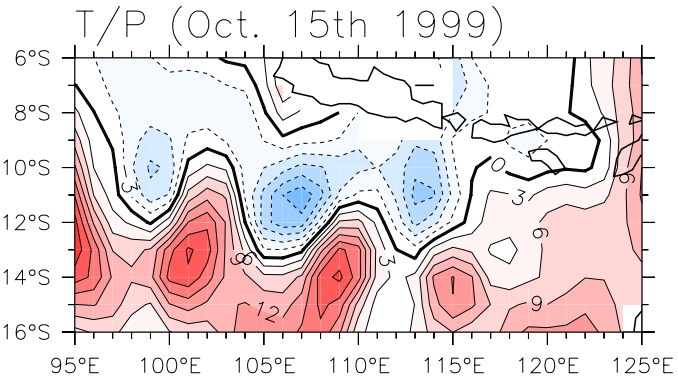

Figure 3. Ten-day-cycle sea-level anomalies from T/P centered on October 15, 1999.

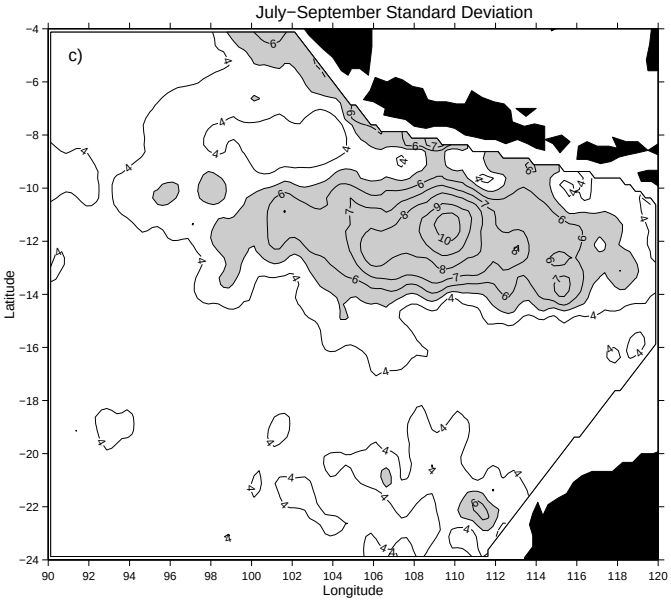

Figure 4. Reproduction of Figure 3c from *Feng and Wijffels* [2002]. Standard deviation of sea-level anomaly during July–September from the 100-day high-pass filtered altimeter data. The shaded region denotes standard deviation larger than 5 *cm*.

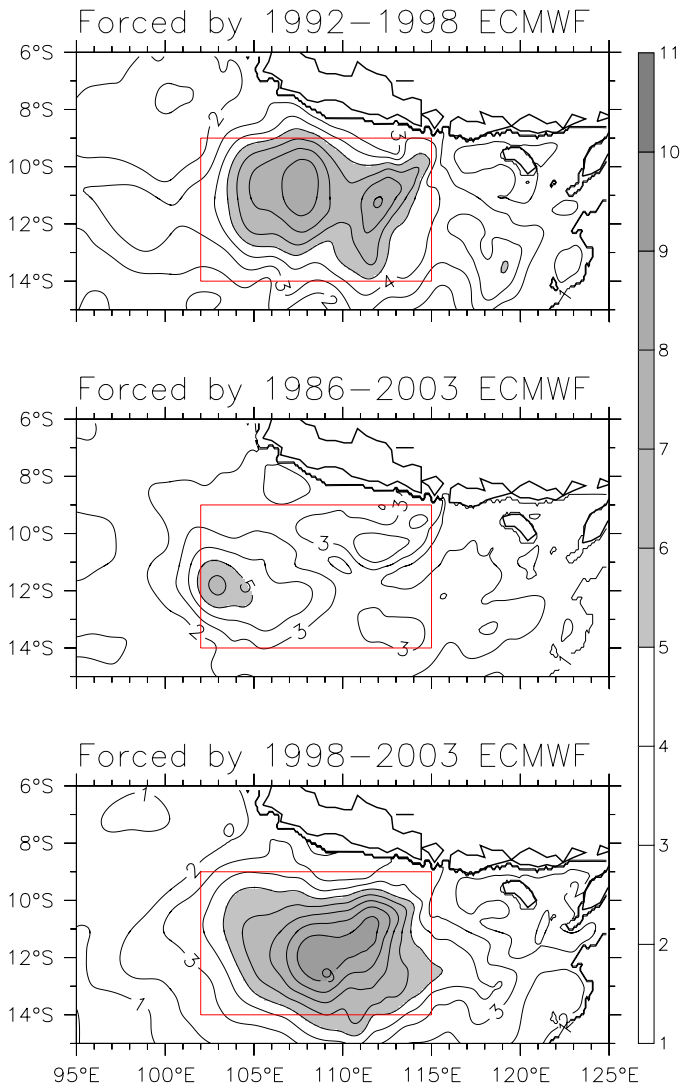

Figure 5. Standard deviation of sea-level anomaly during July–September with seasonal-mean removed. The shaded regions highlight standard deviation larger than 5 *cm*. Each panel is forced by a monthly-mean wind climatology over a specific period: October 1992–December 1998 (Exp. A0; top), 1998–2003 (Exp. W1; middle), and 1998–2003 (Exp. W2; bottom).

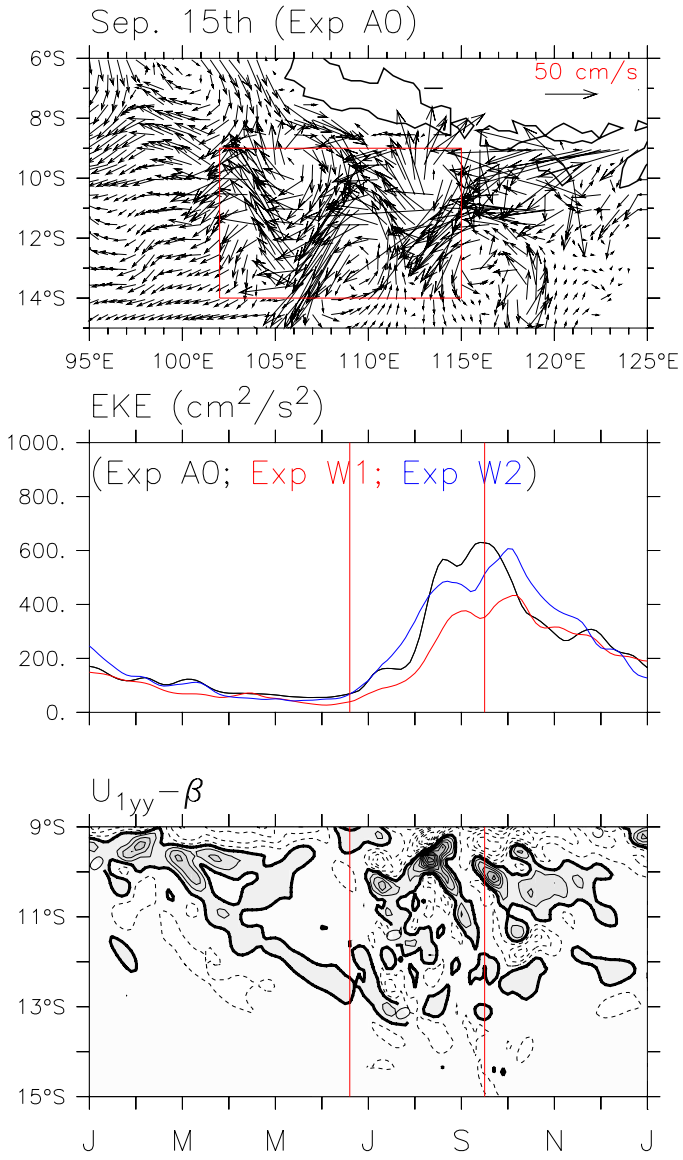

Figure 6. Top: A snapshot of surface flows from the main run. Middle: Layer-1 eddy kinetic energy (black curve) averaged from 102°E to 115°E and from 14°S to 9°S during year 6 of the main run. The two additional curves are from Exp. W1 and Exp. W2 forced by different wind climatologies (corresponding to the lower panels of Figure 5). Bottom: $(\frac{\partial^2 U_1}{\partial y^2} - \beta)$ from the main run, where U_1 is averaged between 110°E and 115°E. For appearence only, a 3-point running mean in time has been applied for both lower panels, and an additional 3-point smoothing has been used in the meridional direction for the bottom panel.

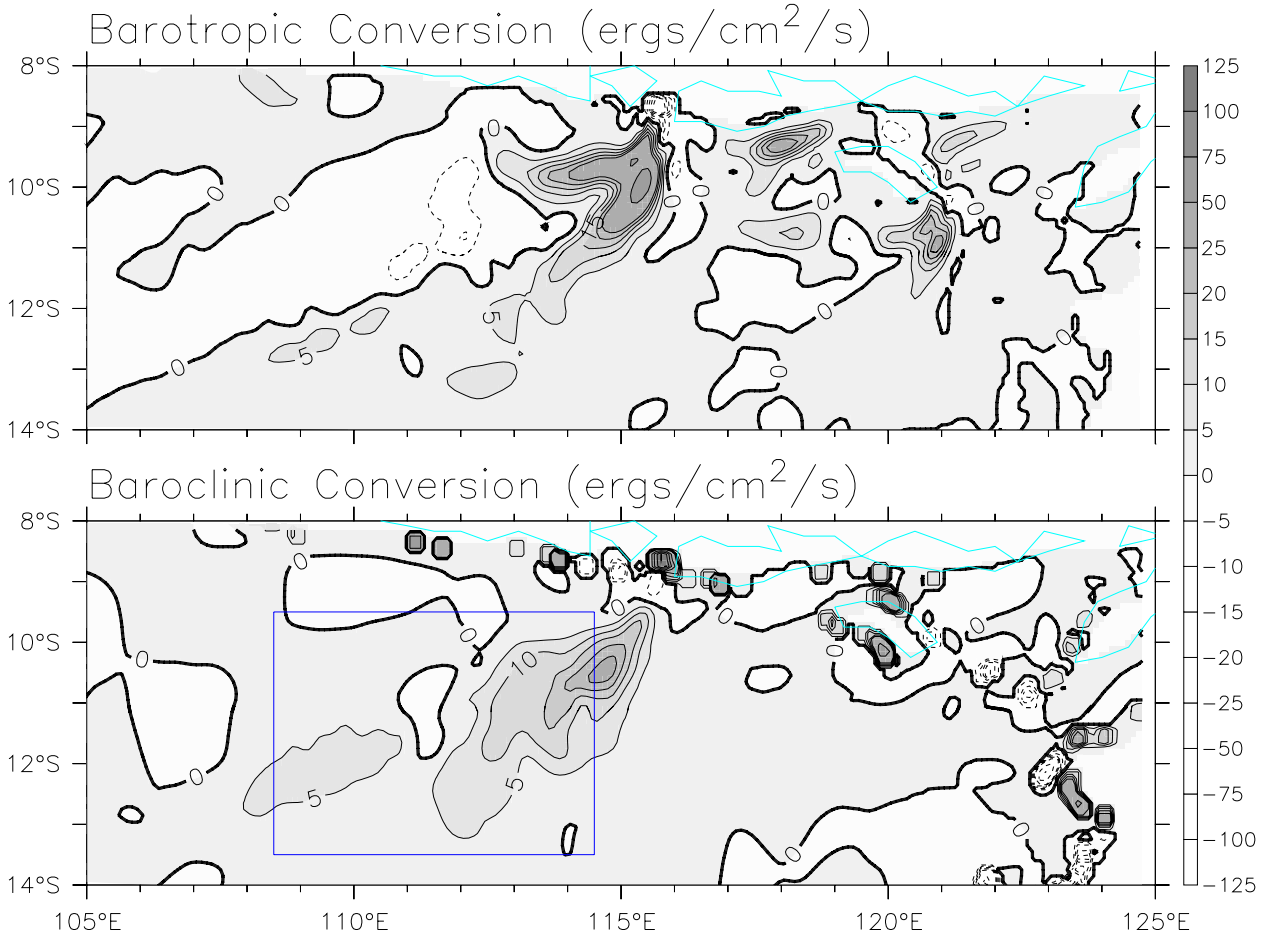

Figure 7. Energy conversions of the main run during the growth period of instabilities (marked by red vertical lines in the lower panels of Figure 6). The maximum barotropic conversion locates just south of the Lombok Strait, and extends southwestward. In addition, there exist two secondary maxima west and south of Sumbar Island, respectively. The baroclinic conversion is also a source, though somewhat weaker than its barotropic counterpart. The blue box marks the area used by *Feng and Wijffels* [2002] for their baroclinic energy calculation.

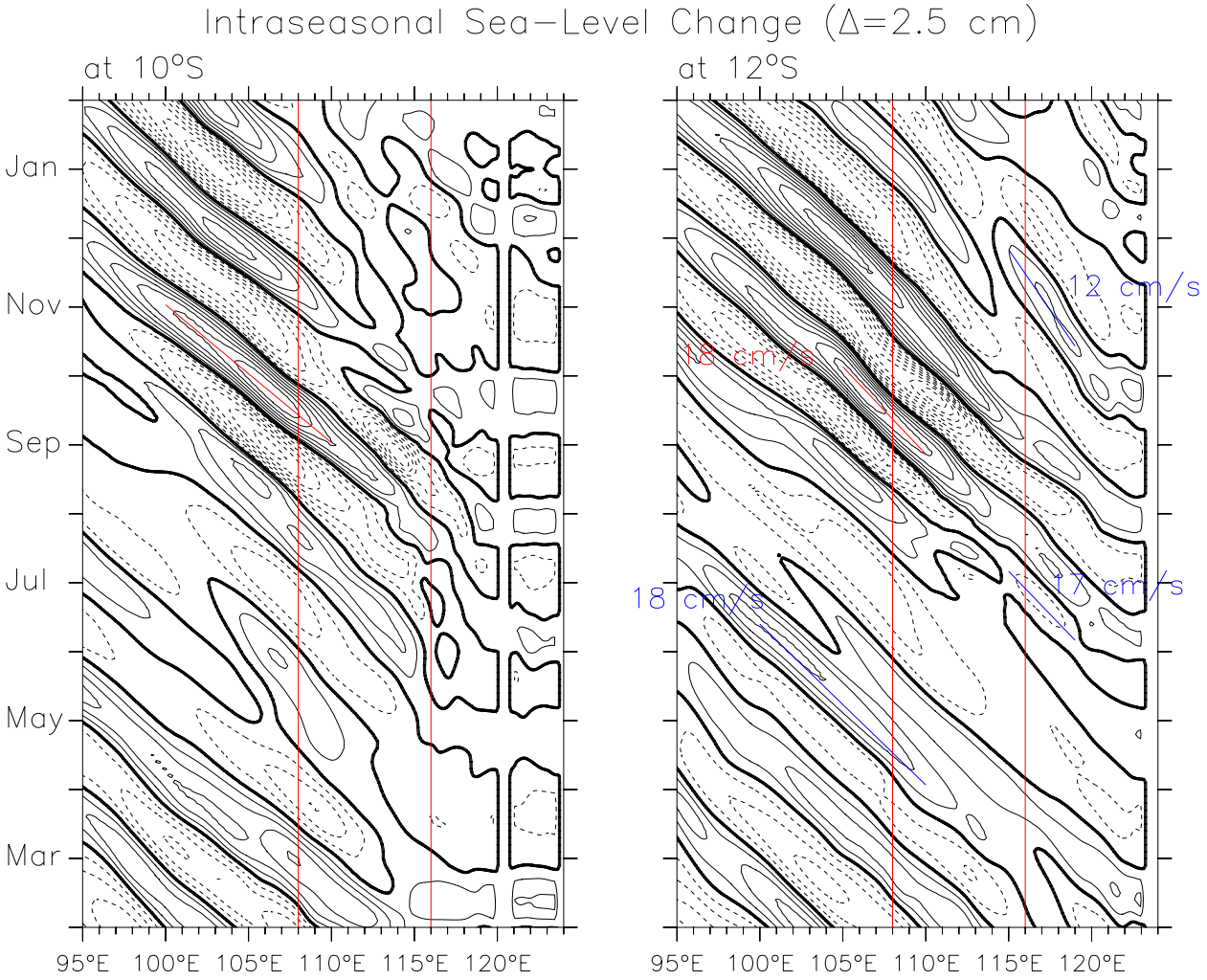

Figure 8. Time-longitude plot of intraseasonal sea-level change along 10°S (left) and 12°S (right). The red vertical lines mark roughly the edges of the generation region as determined by energy conversions in Figure 7, so the eddies to the west of 108°E can be considered as free waves.

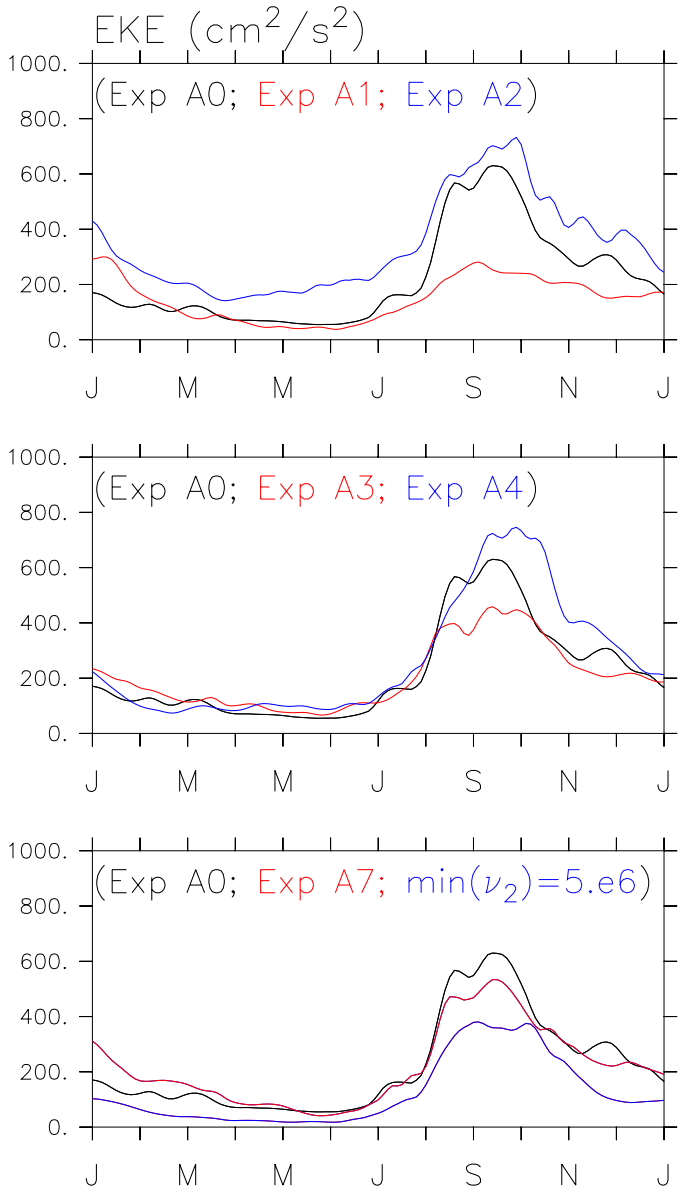

Figure 9. Layer-1 eddy kinetic energy averaged from 102°E to 115°E and from 14°S to 9°S as in the middle planel of Figure 6. The comparison of the three curves in the top panel underlines the importance of the seasonal cycle in M_{Lombok}, as well as of the wind forcing. The middle panel shows the influence of M_{Ombai} and M_{Timor}. The bottom panel illustrates the importance of the inflows' T/S and non-uniform eddy viscosity in the model.

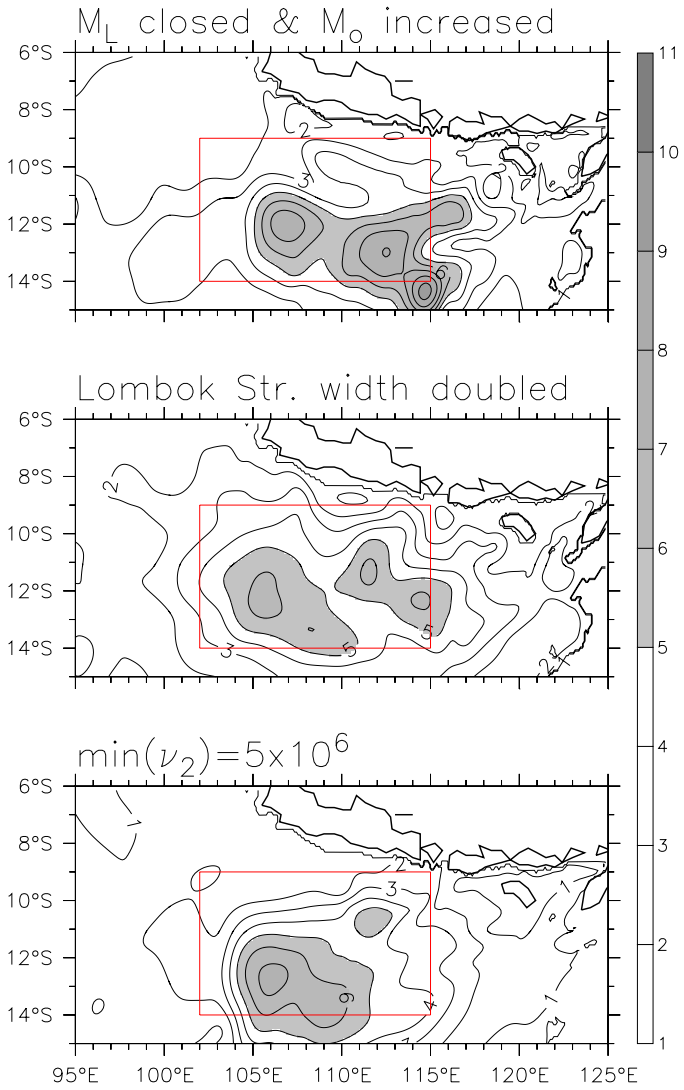

Figure 10. Standard deviation of sea-level anomaly during July–September with seasonal-mean removed. Top: The Lombok Strait in the model is closed, and the observed M_{Lombok} is added to the Ombai Strait. Middle: The Lombok Strait width in the model is doubled, and the observed M_{Lombok} remians unchanged. Bottom: The minimum eddy viscosity is limited to no less than $\nu_2 = 5 \times 10^6\ cm^2/s$.